3D two-photon polymerization of smart cell gelatin – collagen matrixes with incorporated ruthenium complexes for the monitoring of local oxygen tensions

Boudewijn van Der Sanden, Laetitia Gredy, Didier Wion, Olivier Stephan

Version of Record: https://www.sciencedirect.com/science/article/pii/S1742706121003950
Manuscript_5fdf2e73cfd1684376781d92cb755027

3D two-photon polymerization of smart cell gelatin – collagen matrixes with incorporated ruthenium complexes for the monitoring of local oxygen tensions

Boudewijn van der Sanden[1]*, Laetitia Gredy[2], Didier Wion[3] and Olivier Stephan[2]

[1] SyNaBi & Platform of Intravital Microscopy, TIMC-IMAG, CNRS UMR 5525, Université Grenoble Alpes, Grenoble INP, INSERM, Grenoble, France. email: boudewijn.vandersanden@univ-grenoble-alpes.fr
[2] MoVe, Laboratoire interdisciplinaire de physique, CNRS UMR 5588, Université Grenoble Alpes, St-Martin d'Hères, France. emails: laetitia.gredy@univ-grenoble-alpes.fr, olivier.stephan@univ-grenoble-alpes.fr.
[3] Braintech Lab, unité INSERM U1205, Université Grenoble Alpes, Grenoble, France, email: didier.wion@univ-grenoble-alpes.fr

*boudewijn.vandersanden@univ-grenoble-alpes.fr
Fax: +33 (0)4 56 52 00 44

Running title: Smart gelatin – collagen matrixes with linked ruthenium complexes for local $pO_{2matrix}$ measurements.

Abstract

The extra cellular matrix plays a major role in the biomechanical properties of tissues that impact cell behavior and fate. It is therefore crucial to mimic these complex cell-matrix interactions in 3D cell cultures. Here, two-photon polymerization is applied to produce gelatin methacryloyl (GelMA) – collagen matrixes that further enable local $pO_{2matrix}$ measurement, when ruthenium complexes are used as photo-activators. The fluorescence intensity of these complexes has a direct and inverse relationship with the local $pO_{2matrix}$. The 3D structures reached their maximum size in cell culture conditions after 3H with a swelling factor of ~ 1.5. Their shape and the ruthenium fluorescence intensity of the alveoli walls stayed constant for at least 2 weeks in the absence of cells. They were used in time series to monitor the local $pO_{2matrix}$ adjacent to cancer cells during their division, migration and the formation of a tumor tissue mass. At the presence of these cell activities that consume O_2, a significant ~3-fold increase of the ruthenium fluorescence intensity in the alveoli walls was observed. This study demonstrates that online monitoring of the local $pO_{2matrix}$ is possible. The ruthenium complexes provide the bio-optical sensors that are useful for further analysis of cancer and healthy cell energy metabolism in a 3D matrix that better mimics *in vivo* conditions and migration paths. Unraveling the cancer cell metabolic adaptations in a changing micro-environment will help the development of new therapeutic opportunities.

Keywords: GelMA–collagen-ruthenium matrix, two-photon polymerization, 3D cell culture, $pO_{2matrix}$ measurements

Funding: This work was partially funded by the European Innovative Research & Technological Development Projects: NANOMEDICINE EURONANOMED III, project: nAngioDerm and the French

program “Investissement d’Avenir” run by the “Agence Nationale pour la Recherche”; grant “Infrastructure d’avenir en Biologie Santé - ANR11-INBS-0006”.

Abbreviations: ATP, Adenosine TriPhosphate; ECM, extra cellular matrix; GelMA, Gelatin Methacryloyl; GFOGER, glycine-phenylalanine-hydroxyproline-glycine-glutamate-arginine sequence; GFP, Green Fluorescent Protein; RGD, tripeptide Arg-Gly-Asp, TPP, two-photon polymerization.

1. Introduction

The extra cellular matrix (ECM) plays a major role in the biomechanical properties of tissues that impact cell behavior and fate. It is clear that mimicking such cell-ECM interactions with a complex 3D cell culture provides a better system for predicting clinical efficacy of putative therapeutics compared to classical 2D cell culture [1–4]. The choice of the ECM composition depends on the native ECM of a tissue or an organ of interest, for which type I collagen is often the dominant structural protein component. Collagen is biocompatible and bioactive in comparison to their synthetic counterparts and is therefore an ideal material for soft tissue constructs in medical applications [5–7]. Nonetheless, Type I collagen is expensive and its solubility is limited to 30 mg / mL in neutral water medium [8].

Here, we utilized a micron-resolution two-photon polymerization (TPP) 3D micro printer to form 3D ECM matrices. The main advantage of two-photon µ-fabricated structures is the possibility to control 3D architecture with a resolution of a few µm [2,4] in comparison to fibrous assemblies, such as electrospinning [9] that is commonly used to simulate *in-vivo* extracellular environments. Furthermore, the 3D architecture of most spongy or microporous scaffolds using natural and synthetic polymers is heterogeneous [10] and cannot direct cell adhesion, migration and proliferation in a controlled manner as can be achieved with printed scaffolds. For our TPP we added a large amount of water-soluble gelatin to the formulation for 3D printing, which enabled the construction of stable and sufficiently rigid 3D matrices since the formulation had increased viscosity [11,12]. These bioactive matrixes contain integrin cell binding sites, since both collagen that is denatured to gelatin exposes the RGD sequence, and native collagen fibers have the integrin binding site; GFOGER [13–15]. Instead of using pristine gelatin, the strength of the matrices was further improved by increasing the cross-linking density using the commercially available Gelatin methacryloyl (GelMA) that contained additional methacrylate photo-polymerizable groups [12]. The unsaturated methacryloyl groups form covalently cross-linked hydrogels after TPP under mild conditions (laser power ~ 1.5 mW) in the presence of an organometallic complex of ruthenium(II) that functioned as a photo initiator, and eventually became covalently linked to the collagen fiber during the photo-initiated polymerization reactions. Our first approach was to printed GelMa–collagen matrixes with a

simple configuration of homogeneous and fixed alveolus size of 50 µm in order to facilitate the migration of cells inside the matrix pores.

The serendipitous advantage of these ruthenium complexes is that they also function as bio-optical oxygen sensors for localized pO_2 measurements with optimal sensitivity in the physiological range of 0–20% [16]. The fluorescence intensity of these complexes increases when cells consume O_2, since the complexes are quenched in the presence of O_2. Moreover, since the complexes are covalently linked to collagen fibers and do not diffuse freely, the cytotoxicity of these complexes is markedly reduced following the TPP [17].

To our knowledge, this is the first report of covalently linking ruthenium complexes to 3D printed biocompatible and bioactive GelMA–collagen matrixes for direct $pO_{2matrix}$ measurements in 3D cell cultures. Bio-optical oxygen probes, such as ruthenium or porphyrin complexes, have previously been incorporated in nanoparticles [18] or microbeads [19], gels [20], microporous polystyrene-based scaffolds [21] and thin polymer films [22] for direct measurements of oxygen tensions in 2D and 3D cell cultures. A further significant advantage for the TPP of matrixes is stabilizing the ruthenium complexes in the matrix to enable time-series observations of $pO_{2matrix}$. Such time-series measurements are complicated for 3D microscopy of freely moving microbeads and nanoparticles for which the location of the optical oxygen sensors is not fixed.

We demonstrate that 3D soft and biocompatible GelMA–type I collagen matrixes with covalently linked ruthenium complexes can be used for the direct monitoring of the local $pO_{2matrix}$ during cell activity and tumor mass formation in these matrixes. The cells used in this proof-of-concept study are the U87 glioma cell line. The glioma cells express integrins for recognition of the binding sites: GFOGER and RGD, in the matrix [23,24] and are therefore expected to migrate in the alveoli, that mimic the perivascular spaces. Glioma cells migrate here through the whole brain at low energy cost.

2. Materials and methods

2.1 Composition GelMA – collagen- ruthenium gel

A typical hydrogel photoresist solution is obtained by mixing 1 mL of deionized water with 30 mg of collagen (collagen from rat tail, Sigma–Aldrich), 200 mg of gelatin methacryloyl (bloom 300, 80 % degree of substitution, Sigma–Aldrich), and 10 mg of dichlorotris(1,10-phenantroline)ruthenium(II) (Sigma–Aldrich) acting as photo-sensitizer. After gently mixing the solution at ambient temperature for 1H, the temperature is gradually increased to 40 °C to reach a complete dissolution of the components. A strong and solid gel is obtained when the mixture cools to room temperature. This strong hydrogel can be stored for at least 2 months in a refrigerator for later uses.

2.2 3D two-photon polymerization.

A ruthenium organometallic complex (denoted R) was used as photo-initiator assuming that during photo excitation, the non-radiative path leads mainly to the triplet excited state (R*) and the production of singlet O_2 [25]. First, in un-functionalized gelatin [11], intermolecular cross-linking of collagen and gelatin can involve the interaction of singlet oxygen with photo-oxidizable amino acid residues, resulting in hydrogen atom abstraction (R-H) from amino groups of the proteins. The corresponding electron deficient molecule is then able to further react with another amino acid residues to form covalent bonds (crosslinking). Second, in GelMA, R* can also efficiently react with an acceptor leading to $R^{\cdot+}$ radicals able to initiate free radical polymerization of the methacrylate groups [26]. The combination of both processes results in stable 3D structures and decrease the swelling effect over time.

3D cage-like structures (cubic alveoli) were fabricated on a Microlight® (www.microlight.fr) two-photon polymerization 3D micro printer [25], combined with an Olympus inverted microscope using a 40x air objective (Olympus, WD = 180µm, NA = 0.95). The two-photon activation volume is estimated at 4 μm^3. The laser used for the photo-polymerization was a pulsed green Nd-doped yttrium aluminum garnet micro-laser: λ= 532 nm. Prior to printing, the glass coverslips (24 X 24 mm) were washed with acetone and a bind-silane treatment was applied to improve structures adhesion on glass. First, the hydrogel photoresist was gradually heated until 40 °C during continuous stirring. Second, a drop of the photoresist solution was deposited on the cover-glass. Five minutes after returning to ambient temperature, 3D structures were drawn in the solid hydrogel with the laser inside the drop starting at the glass|drop interface. After µ-fabrication, the coverslips were rinsed twice with Phosphate Buffer Solution (PBS) for 30 minutes at ambient temperature and at 40 °C to remove all un-crosslinked materials.

Assemblies of 100 cubic alveoli (50 X 50 µm) were built inside the drops. A hanging base made of 3 µm high pillars (spacing 2 µm) is first manufactured per alveolus to ensure a better adhesion, as shown in fig. 1a. Then, the outer envelope of the alveolus is traced with a 1µm z shift. This form was printed 10 x 10 times with complete overlap for the photo-activation at all horizontal bars except the outermost horizontal bars at the 4 corners of the whole matrix, see fig. 1b. The initial height of the alveoli was limited to 25 µm height, because the swelling factor is 1.5x in the z-direction after washing and incubation in cell culture medium.

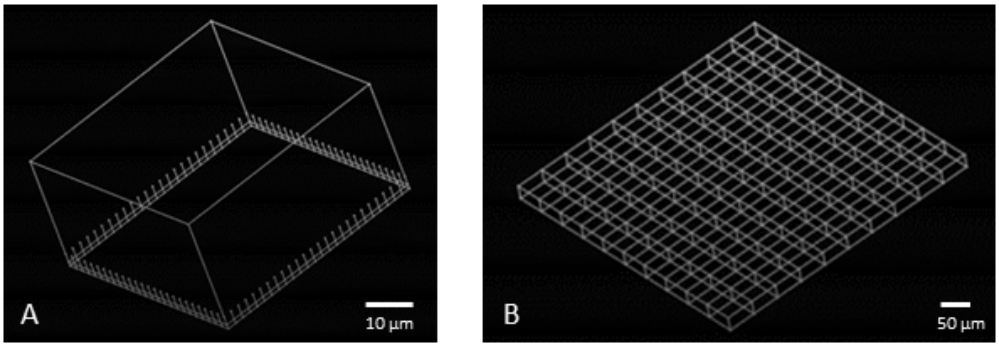

Figure 1a: 3D laser path for a 50 X 50 X 25 µm alveolus including the hanging base. **Figure 1b**: the complete matrix with 10 x 10 alveoli. The manufacturing time for the cubic alveoli assembly is 8 hours.

2.3 Cell culture

Human malignant glioma cells U87MG (ATCC HTB-14), stably transfected with lentiviral vectors expressing either the fluorescent protein GFP (Sigma-Aldrich, SHC003V) or FP635 (Sigma-Aldrich, SHC013V), were cultured at 37°C with 5% CO_2 in Dulbecco's Modified Eagle's Medium (DMEM) 4.5 g/L glucose + GlutaMax, supplemented with 10% fetal bovine serum, and 1% antibiotic solution (10 mg/mL gentamicin, 10 mg/mL streptomycin, 10 000 units/mL of penicillin). For experiments, 1.5 x 10^6cells were seeded on 3D matrixes in 60 x 15 mm cell culture dishes.

2.4 Two-photon microscopy

All experiments were performed on a two-photon microscope (Trimscope II, LaVision BioTec, Bielefeld, Germany) which is coupled to pulsed infrared laser (Insight Deepsea, Micro-Control Spectra Physics, Evry, France) with wavelengths tunable between 700 – 1300 nm. All 3D two-photon images in time were acquired with a 16x objective (N.A. = 0.8, WD = 3mm, Champigny Sur Marne, Nikon, France) using an x-y plane resolution with 1.38 µm/pixel, a typical total image size of 504 x 504 pixels (694 x 694 µm) and interslice distance of 2 µm for z-stack acquisitions. For most 4D acquisitions (3D in time), the time interval between all 27 z-stacks was 4 min with a total acquisition time of 108 min. The wavelength for the simultaneous excitation of the GFP, and the ruthenium complex was λ_{ex} = 900 nm and λ_{ex} = 1100 nm for the red fluorescent protein FP635 if present. The emission filters in front of the PMTs for the green and red channel had respectively the following characteristics: 542 ± 50 nm and 630 ± 50 nm.

A stage-top incubator (Okolab, Pozzuoli, Italy) was used to maintain the O_2, CO_2 and temperature constant to respectively: 19%, 5% and 37°C during the two-photon microscopy experiments. For the normoxic (19% O_2) – hypoxic (1% O_2) cycles, air was exchanged by N_2, but the

CO_2 was kept constant at 5%. The gas mixture and temperature were monitored online every 30s and stored in a datalog file during the whole experiment.

2.5 3D two-photon image treatment and analysis

2.5.1 Matrix swelling studies.

For the whole time series, changes in the alveoli heights were measured at 3 different locations in orthogonal views at the center of the matrix. The mean changes (Δ) of the heights ± their standard deviations (SD) were calculated starting at time 0. The raw data were fit to a one phase exponential association: Y=Ymax*(1-exp(-K*X)), with a half-life of 0.69/K, using GraphPad Prism. 97% of the steady state is reached at 4K.

2.5.2 Local and global analysis of the ruthenium complex fluorescence intensities in time.

These analyses were performed at a single cell level as explained in the following paragraph 2.5.2.1 or as mean intensity changes per slice in a growing tumor mass as described in paragraph 2.5.2.2. Since the linked ruthenium complex concentration and instrument settings may slightly differ between experiments; a comparison between ruthenium fluorescence intensity changes in the presence or absence of cells was made using the same matrix. In a next study, we will perform accurate half-life time measurements of the ruthenium fluorescence quenching using fast FLIM for the quantification of the local oxygen tensions in the matrix ($pO_{2matrix}$) via the Stern-Volmer equation, see [16]. These analyses are independent of the ruthenium complex concentrations.

2.5.2.1 Single cell analysis: The protocol shown in fig. 2, summarizes the relative analysis of ruthenium complex fluorescence signal intensity changes in the alveoli walls in time at the presence of a single cell and correct for movements in the y-direction if necessary.

First, the background of all images was corrected using a rolling ball algorithm in Image-J software: version ImageJ 1.51u, Wayne Rasband, NIH, USA, *http://imagej.nih.gov/ij*, Java 1.8.0_66 (64 bit). Second, in 4D acquisitions of the whole matrix, the first voxel of interest (VOI-1, red color code) was selected in an alveolus that contain an active cell (green GFP signals). Here, the fluorescence signal intensity changes of the alveolus wall next to the cell in VOI-1 were compared to those in a wall of a second voxel (VOI-2, blue color code), which was adjacent or close to VOI-1 and contain no cell.

The volume of the red and blue voxels was similar and was determined as follows: 1) In a merge 3D two-photon image that contain both the U87MG GFP+ cells (green signals) and the matrix (red signals), we selected only the slices of the z-stack that include GFP fluorescent signals of the cell. 2) In 3D two-photon image of only the matrix (red channel), we summed the ruthenium fluorescence

intensities in all these slices (= same slices as in step 1) that cover the whole wall next to the cell. For all z-stacks in the time series (~2H), we checked if the alveolus wall stayed inside the VOI-1, otherwise the voxel size was increased only in the y-direction to include the whole wall despite movements. Then, the whole voxel was moved at the same height in the matrix to an alveolus wall next to VOI-1 that contain no cells and the calculation of the sum was repeated, see above and fig. 2,

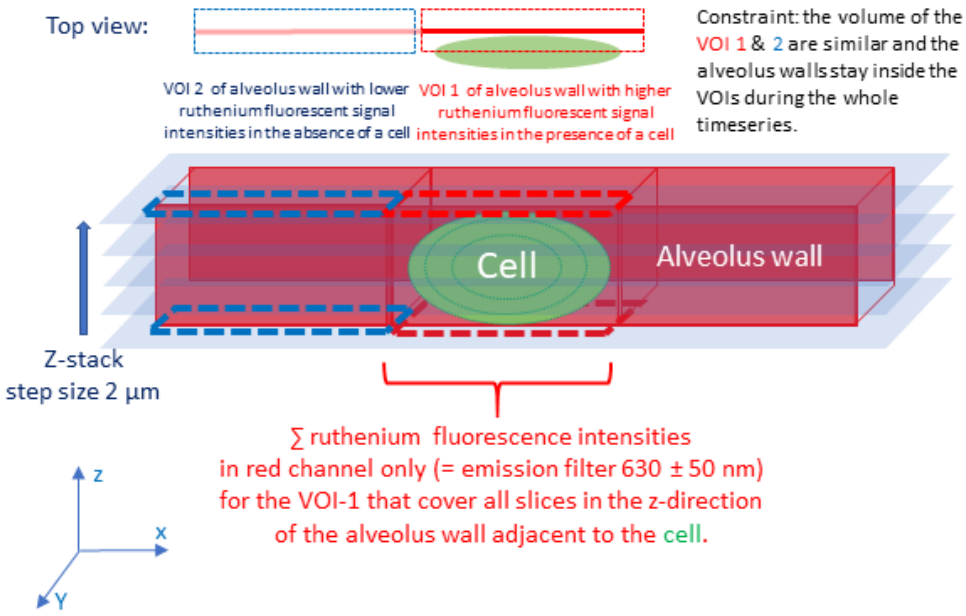

4 & 5.

Figure 2: Summary of two-photon 3D image analysis of the ruthenium fluorescence intensities in the alveolus wall next to a cell (red voxel of interest 1 (VOI-1)) and in an adjacent alveolus wall with no cell (blue voxel of interest 2 (VOI-2 = control)).

2.5.2.2 Tumor mass analysis:

In all experiments, most cells were aligned on the alveoli walls and therefore their surface area better determines the contact area with the alveoli walls than the cell density (number/mm^2). Thus, we assumed that the cell area fraction per slice (%) is correlated to ruthenium fluorescence intensity or to the $pO_{2matrix}$ changes in the tumor mass.

For tumor mass analysis, we calculated the mean ruthenium fluorescence intensity changes per slice for the whole z-stack using ImageJ at different times after cell seeding: day 1, day 8 & day 15. These analyses were completed with estimations of the cell area fractions (%) per slice for the same time points, but only for slices at the top of the matrix that include cells inside their alveoli. The following steps were applied using ImageJ: 1) background correction with the rolling ball algorithm;

2) creation of a substack with only slices that include cells inside their alveoli; 3) segmentation of the U87MG GFP+ cells using the green channel (emission filter 542 ± 50 nm); 4) calculation of the whole cell surface fraction (%) per slice: total cell surface (pixels) / total matrix area (pixels) per slice. The whole area of the matrix was adapted when the latter decreases going from the center to the top of the matrix.

2.6 Statistical Analysis

All statistical analyses were performed using GraphPad Prism (version 3.02). In the matrix swelling studies of paragraph 2.7, a one phase exponential association: Y=Ymax*(1-exp(-K*X)), with a half-life of 0.69/K was used for nonlinear regression. The R^2 value (max. 100%) is used as a statistical measure of how close the data are fitted to the model. In the paragraphs 2.8 and 2.9, differences between the mean fluorescence intensities of the linked ruthenium complexes in the alveoli walls in the absence of in the presence of cell activity were analyzed with the unpaired two-tailed t-test and were significant for p-values < 0.05.

Results

In the first part of the results, the swelling of the GelMA – collagen matrix in DMEM cell culture medium and the complete wash out of the free ruthenium complexes are analyzed (fig. 3). Second, the impact of normoxic – hypoxic cycles on the fluorescence intensities of the linked ruthenium complexes are tested (fig. 4). Third, local changes of the ruthenium fluorescence intensities are shown during human glioma cell division and migration (fig. 5). Finally, the latter is completed with analysis of the mean ruthenium intensity changes per slice in a growing tumor mass inside the matrix during 15 days (fig. 6 & 7).

2.7 Matrix swelling studies

In fig. 3, 3D two-photon microscopic images are shown of the matrix at time 0 (fig. 3a & b) and at 3H (fig. 3c & d) after swelling in DMEM cell culture medium in controlled conditions, see legend. The matrix swelling studies were performed in similar conditions as the *in vitro* studies. This is crucial because parameters such as temperature, pCO_2, pO_2, as well as proteins in the DMEM cell culture medium, which bind to the matrix, can influence the wash-out of the free ruthenium complexes, the swelling rate of the matrix, the pH of culture medium and matrix, and the linked ruthenium fluorescence intensities, respectively.

The maximum size of the matrix was obtained after 3H with a swelling factor of ~1.5 (see fig. 3c.). This factor is estimated as the ratio of the mean matrix height after swelling divided by the mean height before swelling, which is ~ 225/125 pixels. The matrix, which is a hydrogel that consist of a water insoluble polymer network, swelled substantially in aqueous solutions and biofluids.

The top view of fig. 3d, shows that the alveoli walls became softer and more irregular in comparison to fig. 3b, which is the top view of the freshly printed matrix with rigid alveoli walls. The alveoli walls and the borders of the matrix stayed closed after swelling, thus cells only enter the matrix via the top, see *in vitro* studies below. In fig. 3e, changes of the mean height of alveoli walls ± standard deviations were calculated in time from three different measurements using the orthogonal views in the middle of the matrix, see legend for details. Indeed, nonlinear regression analysis confirm that 97% of the steady state was reached after 190 min.

The free ruthenium complexes were washed out in the culture medium after 100 min, resulting in no fluorescence signals of these complexes being detectable after this period. The fluorescence signal intensities of the linked ruthenium complexed in the alveoli walls were measured during 2 weeks after swelling in culture medium and stayed stable over time (results not shown). Thus, ruthenium fluorescence intensity changes in *in vitro* studies hereafter are not due to a loss of ruthenium complexes or a continuous binding of proteins on matrix fibers that may form a growing

protein layer and consequently decrease ruthenium fluorescence intensities in time. Second harmonic generation (SHG) imaging of the matrixes did not reveal SHG-signals of collagen fibers (results not shown). The irreversible denaturation of collagen proteins in gelatin and the photo-activation of the collagen type I fibers most probably disturb the tight alignment of repeating structures within the collagen triple helix. This supramolecular structure is necessary for coherent

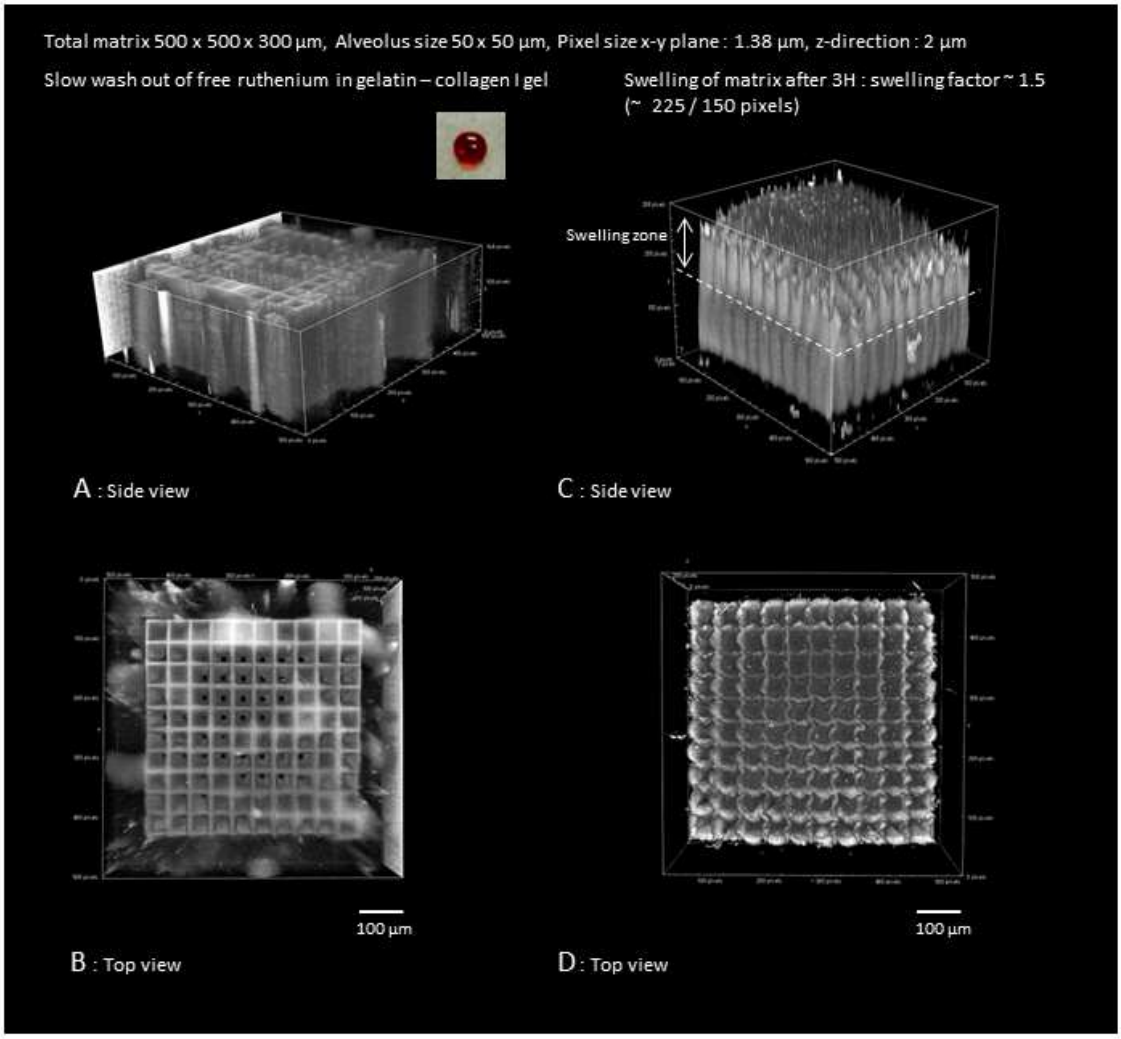

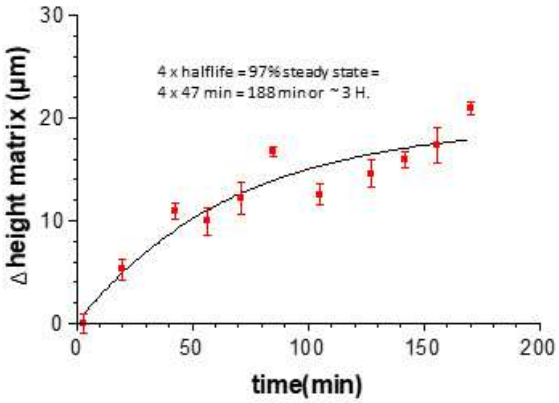

E : Swelling matrix in time. High matrix = mean of 3 heights of alveoli walls as measured in orthogonal views.

amplifications of the SHG signals.

Figure 3: Following in time the swelling of the GelMA - collagen I – ruthenium matrix and wash out of the non-bonded ruthenium complexes directly after immersion in DMEM culture medium at 19% O_2 5% CO_2 and 37°C using an Okolab stage-top incubator. 3D images were acquired on a two-photon microscope (z-stacks: x-y planes 504 x 504 pixels, size 694 x 694 µm, step size 2µm) at an excitation wavelength of 900 nm and a red emission filter (630 ± 50 nm). 3D images were generated using the NIKON software: NIS-elements. **Figure 3a-b:** Top and side view of the 3D matrix with a size of 500 x 500 x 300 µm and an alveolus size of 50 x 50 µm, at time 0. The insert shows the GelMA – collagen I – ruthenium (red staining) gel that contain the matrix after 3D TPP. **Figure 3c-d:** Top and side view of the same 3D matrix at 3H after swelling in DMEM cell culture medium. The maximum size of the matrix is reached at this time with a swelling factor of approximately 1.5. The pixel size = 1.38 µm in the x-y plane and 2 µm (= minimum step size of the z-stack) in the z-direction. **Figure 3e:** The mean of alveoli wall length changes (Δ) in the z-direction in time as measured at 3 different locations in orthogonal views in the middle of the matrix. The raw data were fit to a one phase exponential association: Y=Ymax*(1-exp(-K*X)), with a half-life of 0.69/K, 97% of the steady state is reached at 4K = 189 min, using GraphPad Prism. Best-fit values: YMAX=19,52, K=0,01467, HalfLife= 47,24 min, R^2=0,98.

2.8 The impact of normoxic – hypoxic cycles on the fluorescence intensities of the linked ruthenium complexes.

Our matrix-swelling experiments showed that it is possible to produce stable GelMA-collagen-ruthenium 3D matrixes for which the fluorescence intensities of the linked ruthenium complexes did not change for 2 weeks. In a next step, the sensitivity of the ruthenium fluorescence intensities to normoxic – hypoxic cycles was analyzed for several hours, see fig. 4a. In the stage-top incubator, the pO_2 was varied between 19% and 1 % O_2. Fig. 4a shows a quenching of the normalized ruthenium fluorescence intensities at 19% O_2 and an increase of the later in hypoxic conditions (1 % O_2). It took approximately 60 min to reach a steady-state between the gas concentration above the culture medium and at the high of the matrix, which was fixed on a coverslip at the bottom of an open 60 mm Petri dish filled with DMEM culture medium. For example, see the second hypoxic and third normoxic cycles in fig. 4a.

Before we can confirm that ruthenium fluorescence intensity changes are due to local oxygen tensions in the matrix ($pO_{2matrix}$), a negative control study was performed with fixed dead human glioma U87MG -GFP+ cancer cells that were treated for 30 min with 4% paraformaldehyde, see fig. 4b & c. In fig. 4b, color merged two-photon images of a fixed U87MG GFP+ cell (green signal) next to a bar (red signal) is shown for 30 z-stack acquisitions with a time interval of 4 min. Indeed, the dead cells did not move nor metabolize oxygen and the mean of the ruthenium fluorescence intensity fluctuations during 2H were not significantly different between the alveolus wall next to the fixed cell (red squares) and an adjacent wall without cell (bleu squares). These fluctuations were mainly due to alveoli wall movements in the soft matrix during the z-stack acquisitions and were comparable for both locations, see fig. 4c. This further excludes any substantial Fluorescence Resonance Energy Transfers (FRET effect) from GFP to ruthenium, which would have increased the ruthenium fluorescence intensity at the presence of the GFP+ dead U87MG cell.

In conclusion: Fluorescence intensity changes of the linked ruthenium complexes in the soft gelatin – collagen matrix are related to $pO_{2matrix}$ changes.

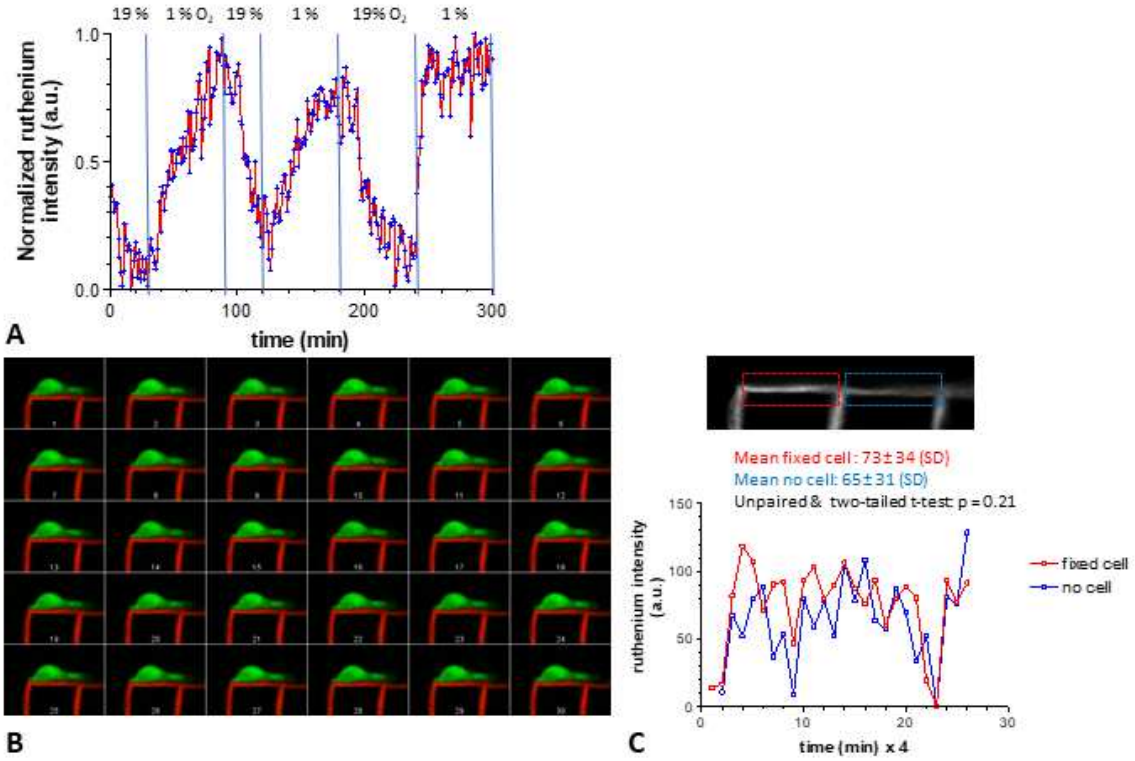

Figure 4a: Testing the ruthenium sensitivity in the GelMA – collagen I matrix in DMEM cell culture medium for O_2 tension changes using normoxic (19% O_2 = AIR) – hypoxic (1% O_2, = mixture of N_2 in AIR) cycles in a stage-top incubator at 37° C. Hypoxic conditions increase the fluorescence intensity of the bonded ruthenium complexes: less quenching of the ruthenium complexes and vice versa for normoxic conditions. It takes approximately 60 min (30 min is too short) to reach an equilibrium between the gaz mixture above the DMEM culture medium and the matrix at the bottom of 60 mm Petri dish. **Figure 4b:** Negative control of ruthenium intensity changes at the presence of a dead U87MG GFP^+ cancer cell at 19% 0_2, 5% CO_2 and 37°C. This negative control is used to measure the ruthenium fluorescence intensity changes in exactly the same experimental conditions as used for the *in vitro* studies in **figures 5 - 7**, but at the presence of a dead cancer cell, which was indeed not moving in comparison to the cells **in figure 5a & d**. The color two-photon image is a merge of the green channel (542 ± 50 nm) with a fixed U87MG GFP+ cells and the red channel (630 ± 50 nm) showing the alveolus wall near the cell in the matrix. λ_{ex} = 900 nm for both acquisitions. The image is a sum of all green and red fluorescence intensity in 11 slices that covers the volume of the whole cell for 30 z-stack acquisitions in time with a time interval in between the stacks of 4 min x 30 z-stacks = 2H. **Figure 4c**: The sum image **at the top** shows the same alveolus wall in only the red channel for the same slices and is used to analyze fluorescence signal intensity changes in time (see graph below) for the ruthenium complex in the wall next to the cell (red dotted rectangle or VOI) and in the wall next to the alveolus of interest with now cell present (blue dotted rectangle). The corresponding fluorescence intensity changes are shown in **the graph** using the same color code. The mean fluorescent intensity values with their standard deviations (SD) were not significantly different between the fixed - and no-cell values ($p< 0.05$, unpaired & two-tailed t-test): $p = 0.21$, using Graphpad Prism for the statistical test.

2.9 Fluctuations of the ruthenium fluorescence intensities during cell division and migration.

The continuous adaption of the cytoskeletal during cell division and cell volume changes during migration are energy consuming processes that need temporary high intracellular concentrations of Adenosine TriPhosphate (ATP). The major source of ATP is the oxidative phosphorylation that increases locally the cell oxygen consumption for this temporary demand [27]. Thus, we hypothesized that these ATP consuming processes, will increase locally the O_2 consumption and consequently decrease the local $pO_{2matrix}$ and the fluorescence quenching of the ruthenium complexes in the alveolus wall adjacent to the cells.

In fig. 5, cell division (fig. 5a-c) and migration (fig. 5d-f) were followed in time using z-stacks acquisitions of the whole matrix during 108 min with a time interval of 4 min.

Cell division: In fig. 5b-c, the changes of the ruthenium fluorescence intensities of the alveolus wall adjacent to the cell division (red color code) were compared to those for a wall at the same location without cell (blue color code). In the first period 1a-b, the cell approached the wall, which increased slightly, but significantly, the ruthenium fluorescence intensities. Period 2 (2a-b) covered the cell division during which the ruthenium fluorescence intensity increased temporary and highly significantly followed by a drop of the intensities after division.

For **cell migration** (fig. 5d-f): the results showed no significant increase of the ruthenium fluorescence intensity for the first period (1a-1b) before the cell entered the alveolus, but the increase became highly significant during and after cell migration in the second period (2a-2b). For both cell processes, the rapid and local $pO_{2matrix}$ changes impacted directly the ruthenium fluorescence intensity changes within minutes (note the 4 min time interval between acquisitions).

In conclusion, the mean ruthenium signal intensity changes for both cell division and migration were highly significantly comparing alveoli walls with and without these processes. These changes were not observed for dead cells (see fig. 4c). Thus, the local O_2 consumption of cells decrease the local $pO_{2matrix}$ and the quenching of the ruthenium fluorescence intensities and can therefore be used to study local and fast dynamic changes in cell oxygen consumption.

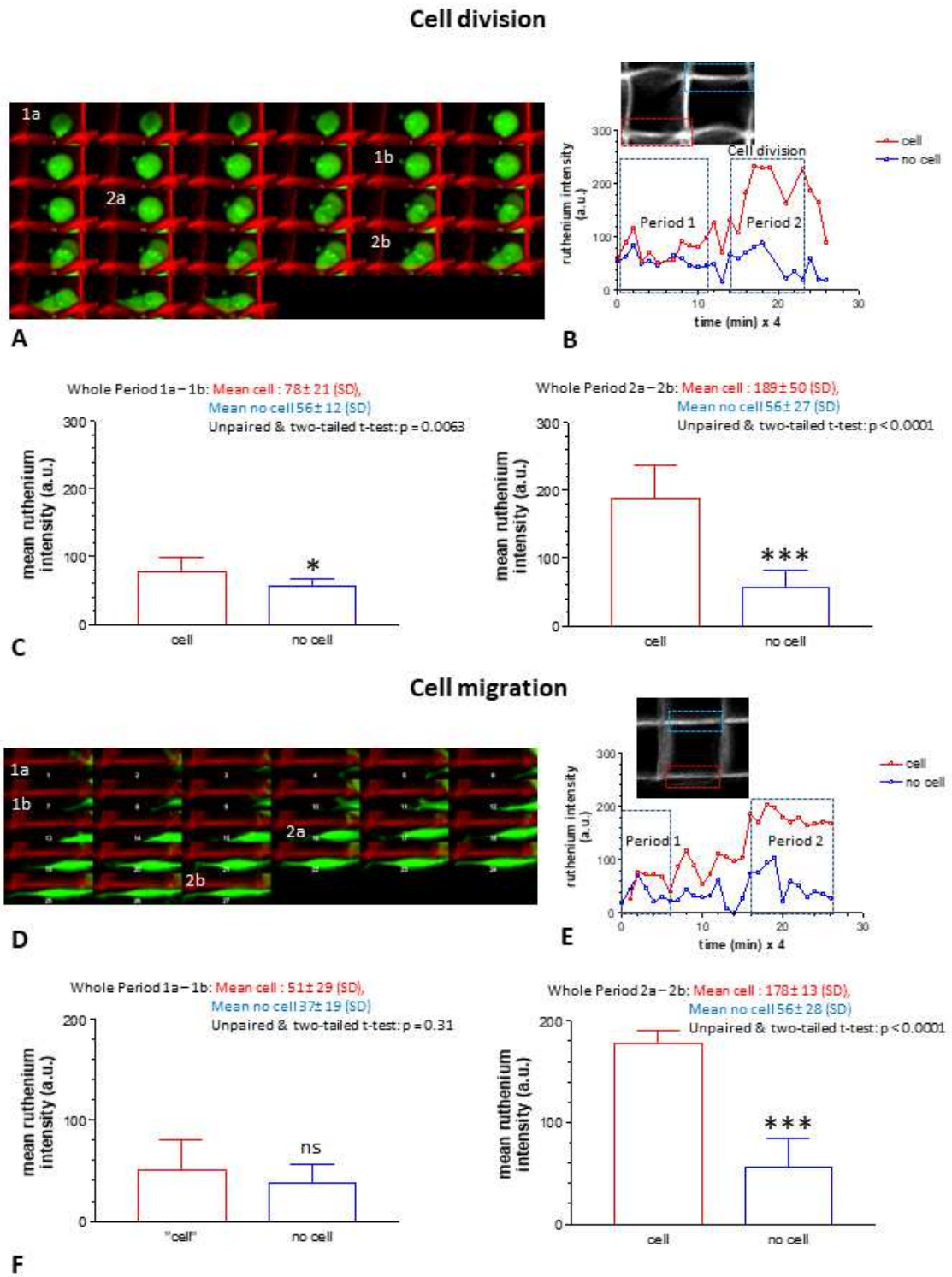

Figure 5: Local ruthenium intensity changes (O_2 consumption) during cancer cell division (**fig. 5a-c**) and migration (**fig. 5d-f**) in the same matrix at 3 days after seeding in DMEM culture medium at 19% O_2, 5 % CO_2 and 37° C. These two activities increase the local O_2 consumption and consequently decrease the local pO_2 tensions and quenching of the ruthenium fluorescence intensities, see **fig. 4a**. **Figure 5a: cell division,** the color two-photon image is a merge of green channel (542 ± 50 nm) with a U87MG GFP$^+$ cell and the red channel (630 ± 50 nm) showing the alveolus wall near the cell division in the matrix, λ_{ex} = 900 nm. The images in the time series are a sum of 15 slices that cover the whole volume of both cells for 27 z-stack acquisitions in time with a 4 min time interval and total acquisition time of 108 min (= 27 z-stacks x 4 min). At the start of the first period (**1a**), the mother cell approaches the bar. At the end of the first period (**1b**), the mother cell prepares the cell division that started in period 2 (**2a**) and finish at **2b**. Both the mother and daughter cells align on the bar of the matrix after division. **In figure 5b:** The signal intensity changes of the ruthenium complex for the red dotted

rectangle (wall next to the cell division) and the blue dotted rectangle (wall in the alveolus without cell) per image in **fig. 5a** are depicted and the mean values ± SD for both periods are calculated and compared in **figure 5c.** Note that the real time on the x-axis is obtained after multiplying the image numbers by 4 min , which is the time interval in between the z-stack acquisitions. For both periods, the mean values were significantly different ($p < 0.05$, unpaired two-tailed t-test): period 1: $p = 0.0063$ and for period 2: $p < 0.0001$ using Graphpad Prism for the statistical test.

Cell migration: figure 5d (see 5a): The images are a sum of 23 slices which covers the volume where the migrating cell is present during the 27 z-stack acquisitions in a time series with a time interval of 4 min and total acquisition time of 108 min (= 27 x 4). In the first period 1a – 1b, the alveolus is empty before the cell enters in the second period and starts to approach the alveolus wall in 2a. At the end of period 2, the cell is aligned on the wall. **Figure 5e:** for the wall next to the cell (red dotted rectangle) and the wall at the opposite site of the alveolus without cell (blue dotted rectangle), the fluorescence signal intensity changes of the ruthenium complex par image in **fig. 5d** are depicted. **Figure 5f:** Indeed, the mean values ± SD in the first period are not significantly different ($p < 0.05$, unpaired two-tailed t-test): $p = 0.31$, but in the second period at the presence of the migrated cell these mean values ± SD became significantly different: $p < 0.0001$ using Graphpad Prism for the statistical test.

2.10 Growing tumor mass and the global oxygen consumption

Here, we followed the formation of a tumor mass in the same matrix during 2 weeks and the effect during growth on the mean ruthenium fluorescence intensity per slice at different heights in the matrix. In fig. 6, the formation of the tumor mass was initiated with green U87MG GFP+ cells at day 0. These green cells occupied most bars (blue signals) in the matrix after 7 days. At day 8, new red U87MG FP635 cells were seeded and observations were extended for 7 supplementary days. The red U87MG cells filled the few empty places in the tumor mass, which was nearly saturated by green U87MG cells at day 8. During this competition study, cells entered more inside the matrix, see fig. 6a & 7a.

In fig. 7, the cell area fractions (%) per slice for all green and red cells were estimated for day 0, day 8 and day 15. These analyses started at slice 92, which was the lowest slice where cells were present inside the alveoli of the matrix at day 15, see fig. 7a. The cell area fractions in between day 8 and day 15 increase after exponential tumor cell growth in deeper slices of the matrix, which correlate to the 2.6-fold increase of the mean ruthenium fluorescence intensity in fig. 6c.

Figure 6a: Time series of U87MG GFP^+ human glioma cancer cell growth in a 3D gelatin-collagen-ruthenium matrix (size: 300 x 300 x 250 µm & alveolus size = 50µm). Two photon microscopic images are the sum of all fluorescence intensity in the whole matrix at day 1 (D1) until day 15 (D15) after cell seeding of green (GFP+) U87MG cells (λ_{ex} = 900 nm) at day 0 and red (FP635) U87MG cells (λ_{ex} = 1100 nm) at day 8 (D8). The color of the matrix (λ_{ex} = 900 nm) is set to blue in comparison to figures 3 & 4, to avoid confusion with the red U87MG cells. Maximum number of slices varied between 115 – 124 with an interslice distance of 2 µm. At day 8, red U87MG human glioma cells are seeded for competition for space analyses in the matrix at day 15. The scale bar = 100 µm. **Figure 6b:** 3D image of the z-stack at day 15, pixel sizes: x-y plane = 1.38 µm, z-direction = 2µm. At day 15, U87MG cells cover nearly the matrix outside and penetrate until a depth of ~ 200 µm inside the matrix (= 100 slices x step size of 2 µm = 200 µm). **Figure 6c:** Graph of mean ruthenium intensity per slice, starting and the bottom of the matrix until the top for matrixes at day 1, day 8 and day 15. After exponential tumor cell growth, approximately the last 38 slices from the top of the matrix at day 15 contain more cells than at day 8, which results in a 2.6-fold increase of the mean ruthenium intensity in the top slices, see further **figure 7**.

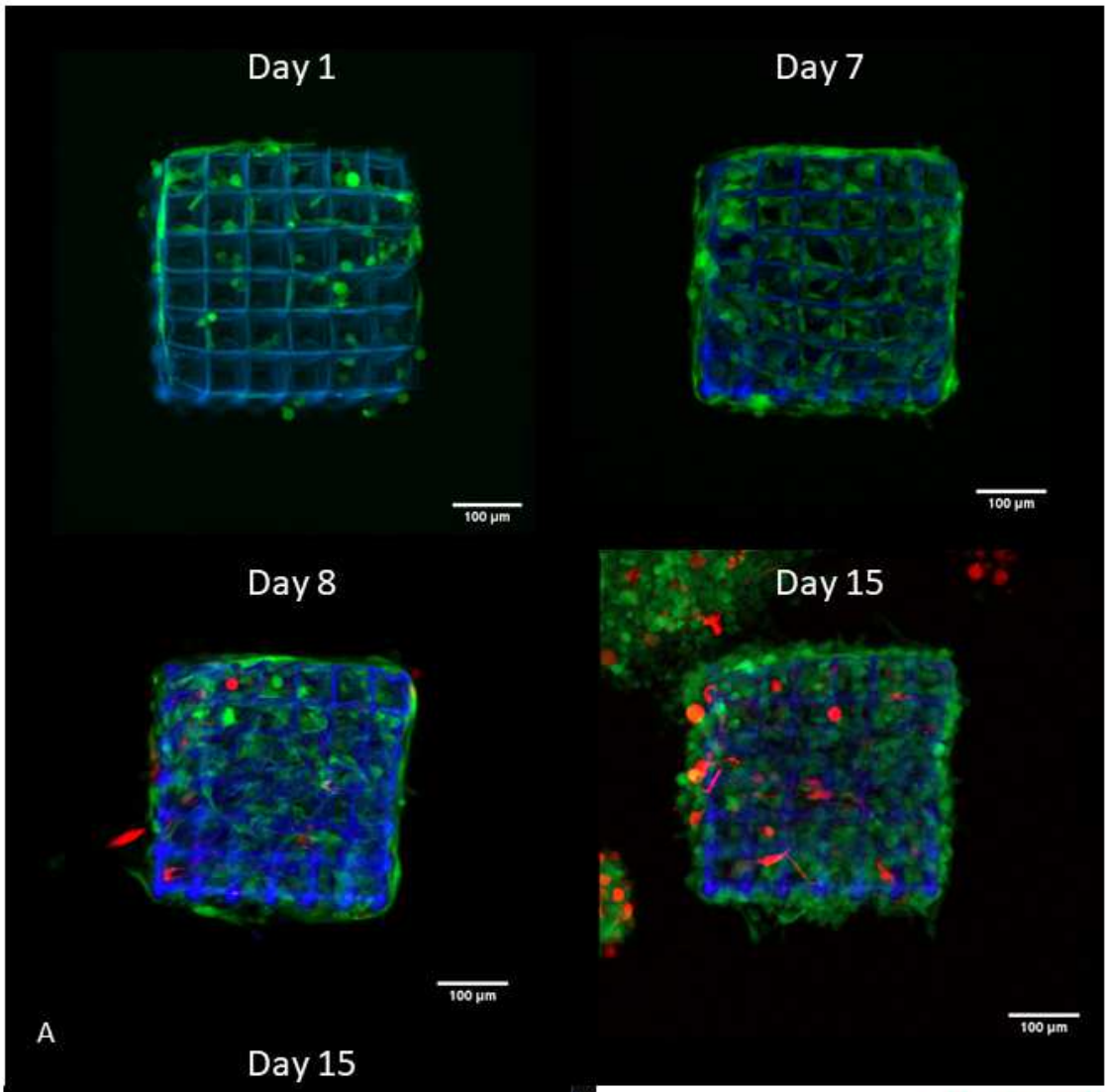
Day 1
100 µm
Day 7
100 µm
Day 8
100 µm
Day 15
100 µm
A

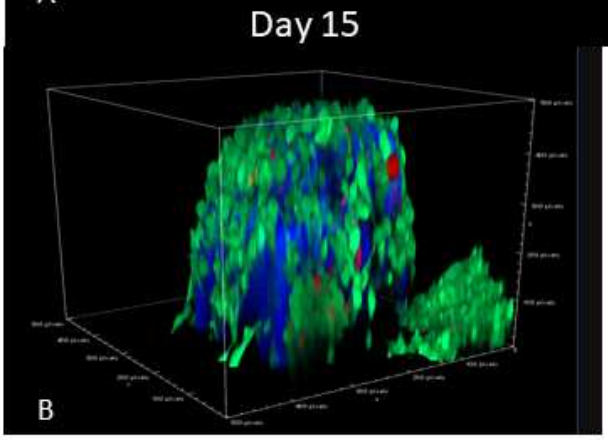
Day 15
B

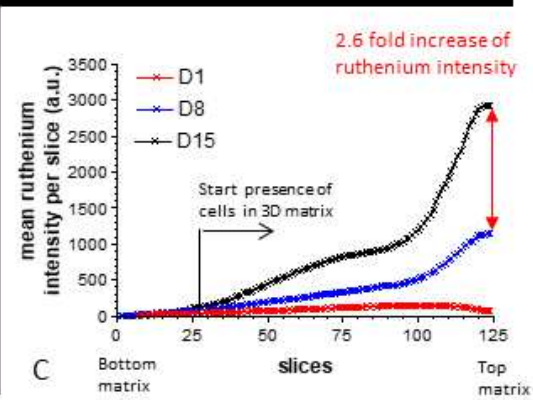
2.6 fold increase of ruthenium intensity
mean ruthenium intensity per slice (a.u.)
3500
3000
2500
2000
1500
1000
500
0
D1
D8
D15
Start presence of cells in 3D matrix
0
25
50
75
100
125
slices
Bottom matrix
Top matrix
C

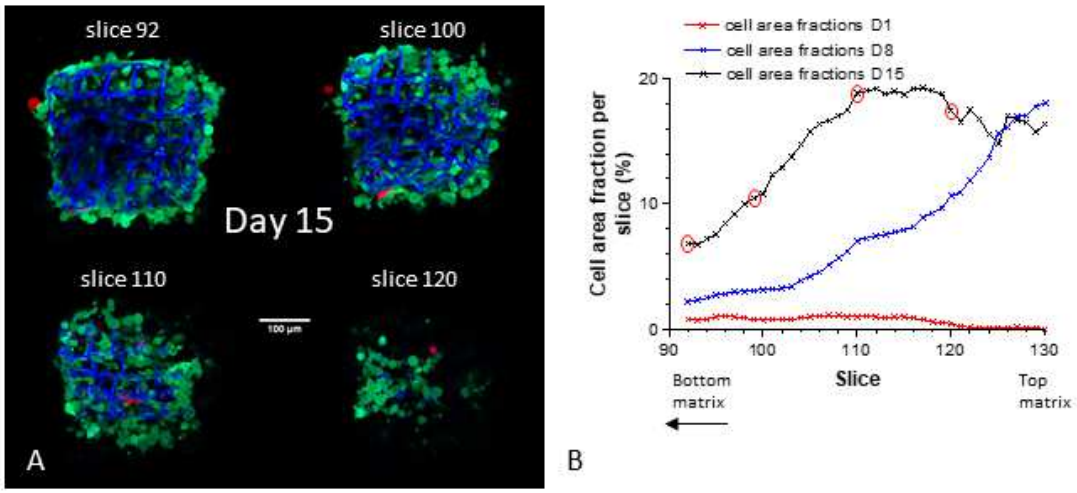

Figure 7a: 4 slices: 92, 100, 110 & 120 of the 3D GelMA-collagen-ruthenium matrix (original size: 300 x 300 x 250 µm & alveolus size = 50µm) containing the U87MG cells at day 15, **see fig. 6a**. The corresponding cell area fractions per slice are depicted in figure 7**b,** see red circles. **Figure 7b:** Plot of the cell area fractions per slice (= cell area / total area matrix) starting at slice 92 until 130 (top matrix) for day 1 (D1), day 8 (D8) and day 15 (D15) after cell seeding. The cell area fractions at day 15 increase after exponential cell growth at deeper layers in the matrix in comparison to the cell fractions at day 8, which is correlated to the 2.6-fold increase of the mean ruthenium fluorescence intensity in fig. **6c**.

3. Discussion

The current study demonstrated the strength of a covalently linked bio-optical sensor ruthenium to a soft matrix of GelMA-collagen for local $pO_{2matrix}$ measurements during cell activity. Direct and non-invasive local measurements of oxygen tensions in a 3D cell culture microenvironment are possible. Here, matrixes were used to better mimic the micro-environment of glioma cells that are known to migrate on collagen fibers in basal lamina in e.g. the perivascular space [24]. In this space, mimicked by cubic alveoli in the matrix, glioma cells showed adhesion, division and migration until occupying most of the cubic alveoli at day 15.

Although, Matrigel™ better reconstructs the basal lamina containing type IV collagen fibers with a sheet-like organization [28], it does not have high proportions of type I collagen filamentous network and hyaluronan that are usually present in *in vivo* tumor microenvironments [29]. Note however, that collagen type IV (and its methacryloyl-substituted derivative) can be added to GelMA-collagen matrix with control over its concentration for fine tuning of the cell-matrix interactions [30]. The matrixes in this study are certainly adapted for other cell types that express integrins for the recognition of the GFOGER and RGD sequences in the matrix [30]. Note that our 3D structures were not degraded during 15 days at cell culture conditions.

In these long time series, no signs of ruthenium cytotoxicity were observed: the glioma U87MG cells divided, migrated and formed already a tumor mass within 8 days. The fluorescence intensity of covalently linked ruthenium complexes in the alveoli walls stayed constant in cell culture medium at the absence of cells and fluctuated at the presence of normoxic (19% O_2) – hypoxic cycles (1% O_2). This indicates that two-photon polymerization did not alter the molecular structure of the ruthenium complex which fluorescence intensity stayed sensitive for $pO_{2matrix}$ changes. This sensitivity was high enough to detect locally a significant ~3-fold increase of ruthenium fluorescence intensities of the alveoli wall at the presence of single cell activity or a growing tumor mass in figures 4-6. The lower signal fluorescence intensity fluctuations that were observed at the absence of cells or at the presence of dead cells in figure 4 were mainly related to slow movements of the soft alveoli walls. Therefore, efforts will be put in the production of more rigid matrixes without changing access to integrin binding sites [31]. In general, the mechanical properties of GelMA-based hydrogels are tunable by varying: 1) the degree of methacryloyl substitution, which was already 80% in this study; 2) increasing the polymer and photo-initiator concentrations; and 3) increasing the photo-cross-linking time, without burning the collagen fibers which occurred for laser exposure times > 24 ms [30].

Further, instrumental instabilities might interfere with ruthenium fluorescence intensity changes due to local O_2 consumption, but the latter and movements never caused a significant (3-fold) increase of the ruthenium fluorescence intensities.

The ruthenium concentration in the alveoli wall might slightly differ between matrixes, although the concentration of photo-activator was kept constant in the initial photoresist formulation at 10 mg/ml. Therefore, the comparison of ruthenium fluorescence intensity changes was only performed inside the same matrix and preferentially between adjacent alveoli at the same location, because the absorption and scattering of the photons depend on the two-photon imaging depth. These difficulties will be overcome using fast FLIM detection of the fluorescence half-life time of ruthenium complexes. Changes in the half-life time before and after O_2 consumption are directly related to $pO_{2matrix}$ changes and are dye concentration-independent as described by the Stern-Volmer equation for fluorescence quenching [16,21].

In 3D TPP hybrid configurations with different alveoli forms and sizes are possible for 3D co-cultures, combining, for example, vascular endothelial cells and adjacent cancer cells. The GelMA – collagen matrix may be filled or combined with other relevant ECM carbohydrate polymers such as hyaluronic acids (HA, [9]). Shrestha et al [32] successfully used TPP for the production of a hybrid HA/gelatin matrix for the growth and attachment of retinal cells. Many different techniques have been applied to generate multi-cellular 3D cultures and tried to address patient specificities; see for review [29,33]. For instance, different cell types were cultured separately in matrixes or hydrogels containing iron oxide particles and magnetically guided together to create a more realistic (tumor) microenvironment.

In the near future, two-photon polymerization of matrixes with different mechanical and biochemical properties can be used in the construction of 3D multicellular cultures with incorporated bio-optical sensors. Here, we focused on local $pO_{2matrix}$ measurements but other bio-optical sensors for the detection of the pH_{matrix} [23], $CO_{2matrix}$ [24], metabolites concentrations [25] or calcium fluxes [26] are available and can possibly be linked to collagen fibers of the matrix for online analysis of the cell (energy) metabolism and intracellular communications [34]. These matrixes can form the basis of *in vitro* drug screening platforms in the development of new therapeutic opportunities that target the oxidative metabolism in proliferative and degenerative diseases. Indeed, impaired glucose uptake and mitochondrial dysfunction play a role in Alzheimer's disease progression [35].

Conclusions: two-photon polymerization of GelMA– collagen matrixes using ruthenium complexes as photo-activator generate stable matrixes in which the covalently linked ruthenium complex can be used for online local $pO_{2matrix}$ measurements during cell activity and formation of a tumor tissue mass.

Credit author statement

Boudewijn van der Sanden: conceptualization, methodology, investigation, validation, resources, formal analysis, visualization, writing original draft, supervision. **Laetitia Gredy**: methodology, investigation, validation. **Didier Wion**: conceptualization, investigation, resources, review and editing. **Olivier Stephan***:* conceptualization, supervision, resources, review and editing.

Acknowledgements

This work was supported by a grant from L' Agence Nationale de la Recherche (ANR-18-ENM3-0004-03) within the framework of the "nAngioderm" project (EuroNanoMed III). The authors also thank Microlight3D for discussions and free assistance with the 3D micro-printer. They further acknowledge the precious help of Prof. D. Martin for improving the grammar and English language.

Data availability

The data that support the findings of this study are available from the corresponding author, upon request.

Declaration of interests

The authors declare that they have no known competing financial interests or personal relationships that could have appeared to influence the work reported in this paper.

References

[1] I. Manini, F. Caponnetto, A. Bartolini, T. Ius, L. Mariuzzi, C. Di Loreto, A.P. Beltrami, D. Cesselli, Role of microenvironment in glioma invasion: What we learned from in vitro models, Int. J. Mol. Sci. 19 (2018). doi:10.3390/ijms19010147.

[2] A.N. Gilbert, R.S. Shevin, J.C. Anderson, C.P. Langford, N. Eustace, G. Yancey Gillespie, R. Singh, C.D. Willey, Generation of microtumors using 3D human biogel culture system and patient-derived glioblastoma cells for kinomic profiling and drug response testing, J. Vis. Exp. 2016 (2016) 1–11. doi:10.3791/54026.

[3] W. Jia, X. Jiang, W. Liu, L. Wang, B. Zhu, H. Zhu, X. Liu, M. Zhong, D. Xie, W. Huang, W.

Jia, S. Li, X. Liu, X. Zuo, D. Cheng, J. Dai, C. Ren, Effects of three-dimensional collagen scaffolds on the expression profiles and biological functions of glioma cells, Int. J. Oncol. 52 (2018) 1787–1800. doi:10.3892/ijo.2018.4330.

[4] G. Rijal, W. Li, Native-mimicking in vitro microenvironment: An elusive and seductive future for tumor modeling and tissue engineering, J. Biol. Eng. 12 (2018) 1–22. doi:10.1186/s13036-018-0114-7.

[5] S.F. Badylak, D.O. Freytes, T.W. Gilbert, Extracellular matrix as a biological scaffold material: Structure and function, Acta Biomater. 5 (2009) 1–13. doi:10.1016/j.actbio.2008.09.013.

[6] M. Meyer, Processing of collagen based biomaterials and the resulting materials properties, Biomed. Eng. Online. 18 (2019) 1–74. doi:10.1186/s12938-019-0647-0.

[7] Gorgieva Selestina; Kokol Vanja; Pignatello Rosario, Collagen- vs. Gelatine-Based Biomaterials and Their Biocompatibility: Review and Perspectives, Biomaterials Applications for Nanomedicine, IntechOpen. (2011) 1–36.

[8] J.M. Unagolla, A.C. Jayasuriya, Hydrogel-based 3D bioprinting: A comprehensive review on cell-laden hydrogels, bioink formulations, and future perspectives, Appl. Mater. Today. 18 (2020). doi:10.1016/j.apmt.2019.100479.

[9] S. Unal, S. Arslan, B.K. Yilmaz, F.N. Oktar, Polycaprolactone / Gelatin / Hyaluronic Acid Electrospun Scaffolds to Mimic Glioblastoma, Materials (Basel). (2020).

[10] M. Abbasian, B. Massoumi, R. Mohammad-Rezaei, H. Samadian, M. Jaymand, Scaffolding polymeric biomaterials: Are naturally occurring biological macromolecules more appropriate for tissue engineering?, Int. J. Biol. Macromol. 134 (2019) 673–694. doi:10.1016/j.ijbiomac.2019.04.197.

[11] O. Stephan, G. Laetitia, Patent: Composition Photosensible activable par absorption multiphotonique pour fabrication tridimentionelle, 2017.

[12] A. Ovsianikov, A. Deiwick, S. Van Vlierberghe, M. Pflaum, M. Wilhelmi, P. Dubruel, B. Chichkov, Laser fabrication of 3D gelatin scaffolds for the generation of bioartificial tissues, Materials (Basel). 4 (2010) 288–299. doi:10.3390/ma4010288.

[13] A.B. Bello, D. Kim, D. Kim, H. Park, S.H. Lee, Engineering and functionalization of gelatin biomaterials: From cell culture to medical applications, Tissue Eng. - Part B Rev. 26 (2020) 164–180. doi:10.1089/ten.teb.2019.0256.

[14] N. Davidenko, C.F. Schuster, D. V. Bax, R.W. Farndale, S. Hamaia, S.M. Best, R.E.

Cameron, Evaluation of cell binding to collagen and gelatin: a study of the effect of 2D and 3D architecture and surface chemistry, J. Mater. Sci. Mater. Med. 27 (2016). doi:10.1007/s10856-016-5763-9.

[15] K.M. Pawelec, S.M. Best, R.E. Cameron, Collagen: A network for regenerative medicine, J. Mater. Chem. B. 4 (2016) 6484–6496. doi:10.1039/c6tb00807k.

[16] N.A. Hosny, D.A. Lee, M.M. Knight, Single photon counting fluorescence lifetime detection of pericellular oxygen concentrations, J. Biomed. Opt. 17 (2012) 016007. doi:10.1117/1.jbo.17.1.016007.

[17] T. Lazarević, A. Rilak, Ž.D. Bugarčić, Platinum, palladium, gold and ruthenium complexes as anticancer agents: Current clinical uses, cytotoxicity studies and future perspectives, Eur. J. Med. Chem. 142 (2017) 8–31. doi:10.1016/j.ejmech.2017.04.007.

[18] A.A. Khan, G.D. Vigil, Y. Zhang, S.K. Fullerton-Shirey, S.S. Howard, Silica-coated ruthenium-complex nanoprobes for two-photon oxygen microscopy in biological media, Opt. Mater. Express. 7 (2017) 1066. doi:10.1364/ome.7.001066.

[19] D. Lambrechts, M. Roeffaers, G. Kerckhofs, S.J. Roberts, J. Hofkens, T. Van de Putte, H. Van Oosterwyck, J. Schrooten, Fluorescent oxygen sensitive microbead incorporation for measuring oxygen tension in cell aggregates, Biomaterials. 34 (2013) 922–929. doi:10.1016/j.biomaterials.2012.10.019.

[20] H.J. Kim, Y.C. Jeong, J. Il Rhee, Encapsulation of tris(4,7-diphenyl-1,10-phenanthroline)ruthenium(II) complex linked with dendrons in sol-gels: Stable optical sensing membranes for dissolved oxygen, Talanta. 76 (2008) 1070–1076. doi:10.1016/j.talanta.2008.05.004.

[21] J. Jenkins, R.I. Dmitriev, K. Morten, K.W. McDermott, D.B. Papkovsky, Oxygen-sensing scaffolds for 3-dimensional cell and tissue culture, Acta Biomater. 16 (2015) 126–135. doi:10.1016/j.actbio.2015.01.032.

[22] B.W.K. Chu, V.W.W. Yam, Sensitive single-layered oxygen-sensing systems: Polypyridyl ruthenium(II) complexes covalently attached or deposited as langmuir-blodgett monolayer on glass surfaces, Langmuir. 22 (2006) 7437–7443. doi:10.1021/la060122q.

[23] A. Ellert-Miklaszewska, K. Poleszak, M. Pasierbinska, B. Kaminska, Integrin signaling in glioma pathogenesis: From biology to therapy, Int. J. Mol. Sci. 21 (2020). doi:10.3390/ijms21030888.

[24] P.G. Gritsenko, O. Ilina, P. Friedl, Interstitial guidance of cancer invasion, J. Pathol. 226

(2012) 185–199. doi:10.1002/path.3031.

[25] K. Iwai, Y. Uesugi, T. Sakabe, C. Hazama, P.I. Photoredox, R.I.E. Reaction, Photopolymerization of Acrylamide, 23 (1991) 757–763.

[26] F. Klein, B. Richter, T. Striebel, C.M. Franz, G. Von Freymann, M. Wegener, M. Bastmeyer, Two-component polymer scaffolds for controlled three-dimensional cell culture, Adv. Mater. 23 (2011) 1341–1345. doi:10.1002/adma.201004060.

[27] B.A. Wagner, S. Venkataraman, G.R. Buettner, The rate of oxygen utilization by cells, 2011. doi:10.1016/j.freeradbiomed.2011.05.024.

[28] M.K. Gordon, R.A. Hahn, Collagens [review], Cell Tissue Res. 339 (2010) 247–257. doi:10.1007/s00441-009-0844-4.Collagens.

[29] W. Asghar, R. El Assal, H. Shafiee, S. Pitteri, R. Paulmurugan, U. Demirci, Engineering cancer microenvironments for in vitro 3-D tumor models, Mater. Today. 18 (2015) 539–553. doi:10.1016/j.mattod.2015.05.002.

[30] D. Loessner, C. Meinert, E. Kaemmerer, L.C. Martine, K. Yue, P.A. Levett, T.J. Klein, F.P.W. Melchels, A. Khademhosseini, D.W. Hutmacher, Functionalization, preparation and use of cell-laden gelatin methacryloyl-based hydrogels as modular tissue culture platforms, Nat. Protoc. 11 (2016) 727–746. doi:10.1038/nprot.2016.037.

[31] N. Davidenko, C.F. Schuster, D. V. Bax, N. Raynal, R.W. Farndale, S.M. Best, R.E. Cameron, Control of crosslinking for tailoring collagen-based scaffolds stability and mechanics, Acta Biomater. 25 (2015) 131–142. doi:10.1016/j.actbio.2015.07.034.

[32] A. Shrestha, B.N. Allen, L.A. Wiley, B.A. Tucker, K.S. Worthington, Development of High-Resolution Three-Dimensional-Printed Extracellular Matrix Scaffolds and Their Compatibility with Pluripotent Stem Cells and Early Retinal Cells, J. Ocul. Pharmacol. Ther. 36 (2020) 42–55. doi:10.1089/jop.2018.0146.

[33] L.J. Bray, D.W. Hutmacher, N. Bock, Addressing Patient Specificity in the Engineering of Tumor Models, Front. Bioeng. Biotechnol. 7 (2019) 1–36. doi:10.3389/fbioe.2019.00217.

[34] B. Van Der Sanden, M. Dhobb, F. Berger, D. Wion, Optimizing stem cell culture, J. Cell. Biochem. 111 (2010) 801–807. doi:10.1002/jcb.22847.

[35] V. Van Der Velpen, T. Teav, H. Gallart-Ayala, F. Mehl, I. Konz, C. Clark, A. Oikonomidi, G. Peyratout, H. Henry, M. Delorenzi, J. Ivanisevic, J. Popp, Systemic and central nervous system metabolic alterations in Alzheimer's disease, Alzheimer's Res. Ther. 11

(2019) 1–12. doi:10.1186/s13195-019-0551-7.

gelatin methacryloyl
Type I collagen
Ruthenium complex

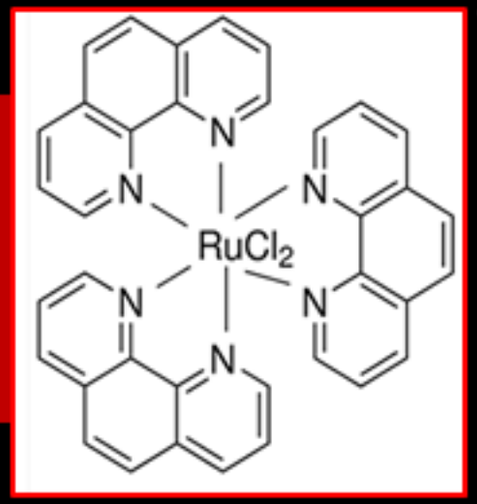

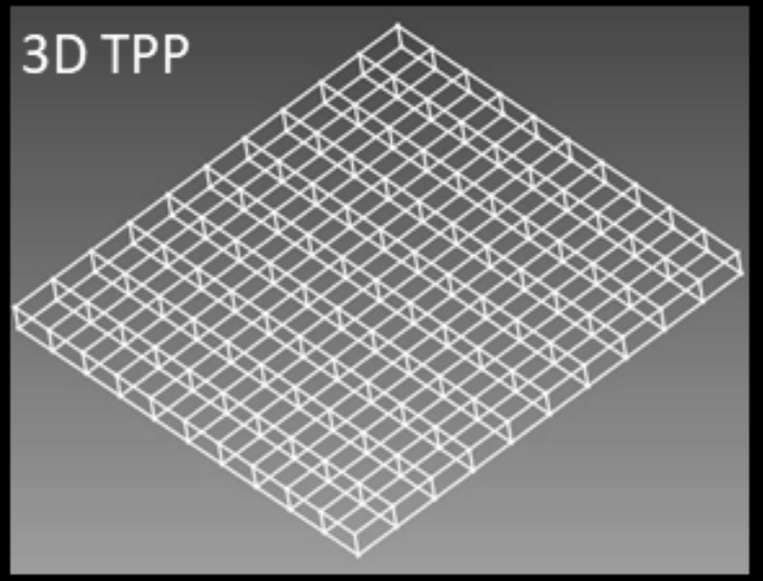

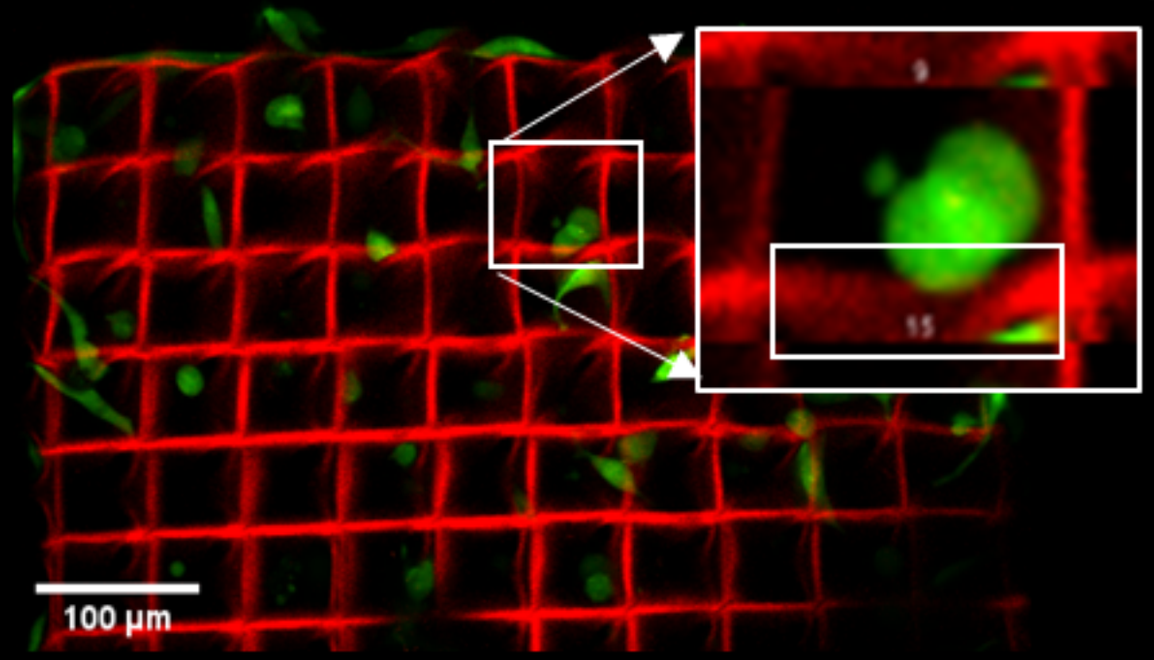

Ruthenium Intensity